

# Improved Ferrite Number Prediction Model that Accounts for Cooling Rate Effects — Part 1: Model Development

*Details of a prediction model based on a neural network system of analysis are described*

BY J. M. VITEK, S. A. DAVID, AND C. R. HINMAN

**ABSTRACT.** A new model, ORFN (Oak Ridge Ferrite Number), has been developed for predicting ferrite content in stainless steel welds. For the first time, ferrite content is predicted quantitatively as a function of alloy composition and cooling rate. The model is based on a neural network analysis of existing data supplemented with newly generated data. This paper describes the details of the model development. The procedure used to calculate the cooling rate in a simple but effective manner is presented. This paper also describes the necessary procedures that were used to convert volume percent ferrite measurements to Ferrite Number. Finally, the procedures used to identify the optimum neural network architecture are outlined. Results from the model, as well as an assessment of the prediction accuracy and comparison with predictions of other models are presented in a companion paper (Part 2). The model is equally valid for austenitic stainless steels and duplex stainless steels, as well as for both conventional arc welding and high cooling rate conditions prevalent during high energy beam welding such as laser beam welding and high-speed arc welding.

## Introduction

Stainless steel welds characteristically consist of a two-phase austenite plus ferrite microstructure. Ferrite levels may vary from a few percent in austenitic stainless steel welds to more than 50% in duplex stainless steel welds. The ability to predict the ferrite content in these welds is essential for many reasons. To a large extent, the final ferrite content determines a weldment's properties such as strength,

toughness, corrosion resistance, and long-term phase stability. In addition, ferrite content is a useful indicator of the mode of solidification and the hot-cracking propensity, which is strongly influenced by whether the alloy solidifies in the primary austenitic or primary ferritic mode. Electrode manufacturers as well as consumers often use Ferrite Number (FN), a measure of the ferrite content, as an alloy specification in order to ensure that weldments contain a desired minimum (or maximum) ferrite level. The need to predict ferrite content is also important in stainless steel castings (although many of the present results can be extended to castings, this paper will be restricted to the consideration of stainless steel welds only).

Over the years, various models have evolved to try to accurately predict the ferrite content in stainless steel welds. Constitution diagrams have been developed that convert the alloy composition into two factors, a chromium equivalent ( $Cr_{eq}$ ) and a nickel equivalent ( $Ni_{eq}$ ). The former contains alloying elements that influence the microstructure in the same way as chromium, i.e., they are ferrite stabilizers, while the latter contains elements that behave as nickel, i.e., as austenite stabilizers. The constitution diagrams display ferrite levels as a function of these chromium and nickel equivalents. An early version of such a diagram that has been used for

welding is the Schaeffler diagram (Ref. 1). Since the introduction of the Schaeffler diagram, several modifications and improvements have been proposed (Refs. 2–7). Corresponding constitution diagrams for stainless steel castings have also been proposed (Refs. 8, 9). The various versions of constitution diagrams differ primarily in the coefficients that are used to convert the alloy composition into the  $Cr_{eq}$  and  $Ni_{eq}$  and their range of applicability. An extensive review is given in Ref. 5. The most recent version of the constitution diagram is the WRC-1992 diagram (Ref. 7). The equations for the  $Cr_{eq}$  and  $Ni_{eq}$  factors in the WRC-1992 diagram are

$$Cr_{eq} = Cr + Mo + 0.7Nb \quad (1a)$$

$$Ni_{eq} = Ni + 35C + 20N + 0.25Cu \quad (1b)$$

where the elemental symbols represent the weight percent (wt-%) of each element.

A major shortcoming of the commonly used constitution diagrams is the fact that the influence of alloying elements on ferrite content is independent of the alloy composition and the presence or absence of other alloying elements, as reflected by the constant coefficients in the chromium and nickel equivalent expressions (Equations 1a and 1b, and Ref. 7).<sup>1</sup> Clearly, this restriction does not represent real behavior very well. For example, the effect of carbon should be very different depending on whether carbide-forming elements are present or not. However, with constant factors, carbon's effect is the same for all levels of carbon and for all combinations with other alloying additions. As another example, the dependence of the

## KEY WORDS

Ferrite Number  
Neural Network  
Duplex Stainless Steel  
Austenitic Stainless Steel  
Ferrite Content  
Cooling Rate  
Alloy Composition  
Constitution Diagram

*J. M. VITEK and S. A. DAVID are with Oak Ridge National Laboratory, Oak Ridge, Tenn. C. R. HINMAN, formerly an intern at Oak Ridge, is now at Syracuse University, Syracuse, N.Y.*

*Paper presented at the AWS Annual Meeting, March 4–7, 2002, Chicago, Ill.*

*1. Some earlier constitution diagrams included composition-dependent parameters (see Refs. 2 and 5), but these apply over restricted composition ranges. In diagrams with constant coefficients (e.g., WRC-1992), composition-dependent parameters were deemed statistically insignificant.*

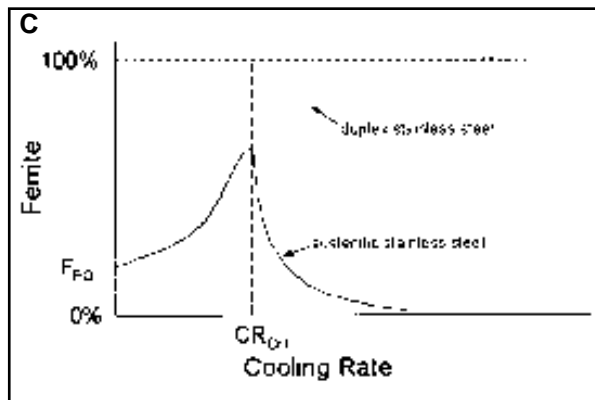
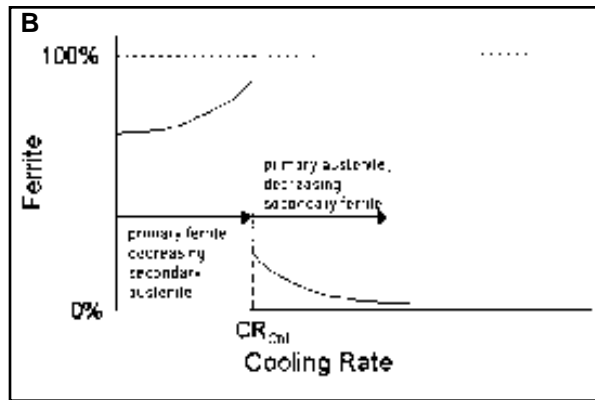
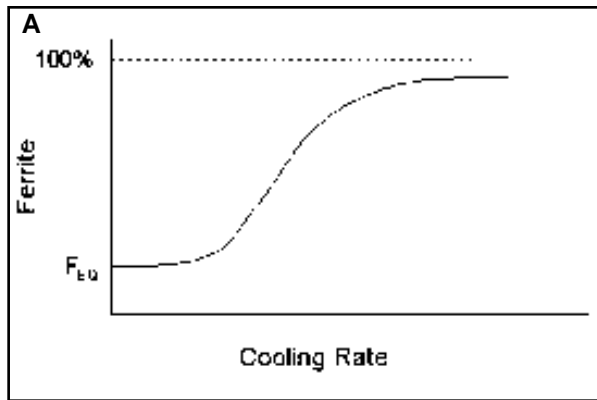


Fig. 1 — Schematic diagram showing the effect of cooling rate on room temperature residual ferrite content. A — Variation in ferrite content as a function of cooling rate due to the change in the degree to which solid-state transformation of ferrite to austenite takes place (fixed amount of ferrite after solidification is assumed). B — Variation in ferrite content immediately after solidification as a function of cooling rate showing the abrupt effect of a change in the primary solidification mode from primary ferrite to primary austenite formation at a critical cooling rate  $CR_{crit}$ . C — Combined effect of cooling rate that takes account of the rate-dependent, solid-state transformation shown in A and the solidification mode change shown in B. For a duplex alloy, the change in solidification mode is not possible and the behavior beyond  $CR_{crit}$  is shown by the dotted line.

effect of manganese on the alloy composition has been noted before (Refs. 10, 11), but these composition-dependent effects have not been included in the most recent diagrams. This limitation has been removed in two new alternatives to traditional constitution diagrams. One recently developed model, the Function Fit Model, considers the difference in free energy between ferrite and austenite as a function of composition (Ref. 12). In this method, the difference in free energy between ferrite and austenite was calculated as a function of composition and this was related to the FN. A regression analysis was used to determine the coefficients associating the FN with the free energy change. It was found that this approach was comparable in accuracy to that of the WRC-1992 diagram.

The second approach is based on an artificial neural network analysis (Refs. 13–15). Neural networks are ideally suited to improve the flexibility, robustness, and accuracy of ferrite predictions because they make use of nonlinear regression methods. The identification of complex trends due to elemental interactions is straightforward with the use of neural networks, whereas they are extremely difficult or impossible to identify by standard regression analyses. The FNN-1999 model, developed with the same data as the WRC-1992 constitution diagram, was shown to reduce prediction errors by as much as 40% (Refs. 13, 14). Furthermore, composition-dependent effects of alloying elements were taken into account and the consequences of this were clearly demonstrated (Ref. 14). A more recent model, which is also based on neural networks, also demonstrates significant improvements compared to the WRC-1992 constitution diagram (Ref. 15).

Another major shortcoming that is present in the traditional constitutional diagrams as well as the newer models, including the recently developed neural network models, is the absence of any consideration of welding conditions and how they may influence the ferrite content of welds. In particular, the weld cooling

rate will have a significant effect on the final ferrite content. There are two ways in which cooling rate will influence the ferrite content: 1) cooling rate will alter the extent of the diffusion-controlled transformation of ferrite to austenite during cooling in the solid state, and 2) it may influence the solidification behavior. Let us examine these two effects in greater detail. For the effect of cooling rate on the solid-state transformation of ferrite to austenite, consider the case of primary ferrite solidification. At the later stages of solidification, some secondary austenite solidification in the interdendritic regions may take place. In any case, during subsequent cooling, the ferrite stability decreases with respect to austenite, resulting in the diffusion-controlled transformation of ferrite to austenite. If there is sufficient time to allow this process to go to completion, the final ferrite content at room temperature will be the equilibrium amount. However, as the cooling rate is increased, the transformation will be suppressed to an ever-increasing degree, resulting in a higher, nonequilibrium residual ferrite content. This behavior is shown schematically in Fig. 1A, where a fixed amount of ferrite (nearly 100%) is assumed to be present immediately after solidification. At the lowest cooling rates, the as-solidified ferrite can transform to austenite during cooling and at room temperature the equilibrium ferrite content is present, denoted by  $F_{EQ}$  ( $F_{EQ}$  may be 0 for some alloys). With increasing cooling rate, the solid-state transformation is suppressed and the residual ferrite content increases. At the

highest cooling rates, the ferrite content may approach 100%, depending upon the alloy composition and the extent to which secondary austenite forms during solidification. Although the degree to which the solid-state transformation is suppressed at high cooling rates has not been studied extensively, the change in ferrite content in duplex stainless steels with increasing cooling rate is well known.

The second way in which cooling rate may influence the final ferrite level is by altering the mode of solidification. This behavior has been studied by many investigators in recent years. They found rapid solidification of austenitic stainless steels, as found during laser welding, for example, can alter the solidification mode so alloys that normally solidify in the primary ferrite mode may solidify in the primary

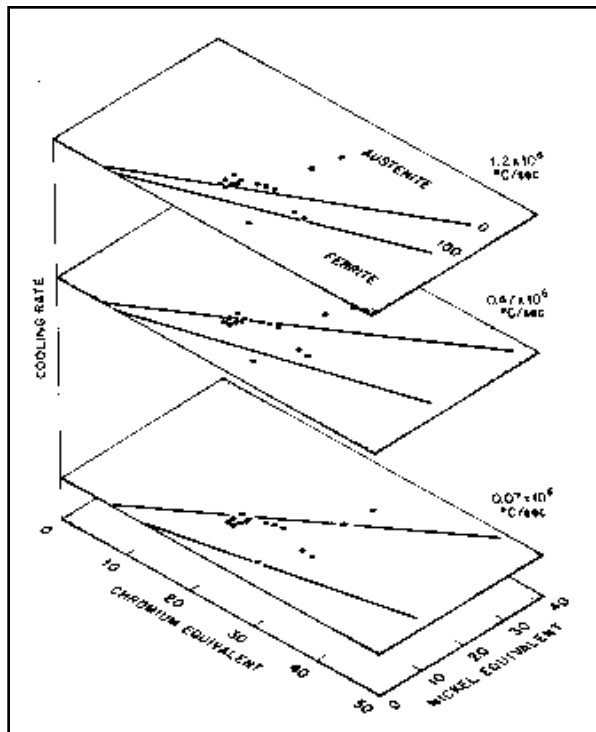


Fig. 2 — Schematic constitution diagram proposed by David et al. (Ref. 18) that qualitatively shows the effect of cooling rate on FN.

austenite mode instead (Refs. 16–23). This behavior is shown schematically in Fig. 1B, where the ferrite content immediately after solidification is plotted vs. cooling rate. For this example, primary ferrite solidification is assumed to take place at low cooling rates. As the cooling rate increases, the degree of solute segregation during ferrite solidification decreases, leading to a decrease in the extent of secondary austenite solidification and a corresponding increase in ferrite content. Beyond some critical cooling rate  $CR_{crit}$ , the solidification mode changes from primary ferrite to primary austenite and a sudden drop in ferrite content will result. However, even if the solidification mode changes to primary austenite, some secondary ferrite solidification can be expected and so the ferrite level does not reach 0 immediately. At still higher cooling rates, secondary ferrite solidification will be suppressed and eventually a 100% austenitic structure should prevail, as shown. The switch in the primary solidification mode from ferrite to austenite will be composition dependent. In some alloys such as duplex stainless steels, the primary austenite solidification option will never be allowed.

The combined effect of solidification mode changes and sluggish solid-state transformations is shown in Fig. 1C. A fairly abrupt transition at  $CR_{crit}$  is shown, although experiments have shown that,

over a limited cooling rate range, mixed mode solidification may be found (Ref. 18). For those alloy compositions that contain high levels of ferrite stabilizers, such as duplex stainless steels, the change in solidification mode never occurs and high cooling rates will result in 100% ferritic microstructures, as shown by the dotted line in Fig. 1C.

The effect of cooling rate on the ferrite content was described qualitatively in the work of David, Vitek, and Hebble (Ref. 18). They showed a schematic, modified constitution diagram in which the two-phase ferrite + austenite field shrunk with increasing cooling rate. Their qualitative depiction of the cooling rate effect is reproduced in Fig. 2. The purpose of the present study was to develop a quantitative model for ferrite prediction in stainless steel welds that accounts for cooling rate effects. The approach that was used was based on the neural network analysis in Refs. 13 and 14. The earlier neural network analysis was expanded to include cooling rate as well as composition as inputs to the model. The nonlinear regression neural network models are sufficiently robust to properly model the complex behavior during solidification and subsequent cooling, taking into account the potential for solidification mode changes and the cooling-rate-dependent diffusion transformation behavior. This paper describes the details of the network development and the generation of the data that were used to train and test the network. In Part 2, the results of the model calculations are presented (Ref. 24). As shown in Ref. 24, the neural network model that emerged from this study, called ORFN for Oak Ridge Ferrite Number, quantitatively describes all the features that have been illustrated schematically in Fig. 1.

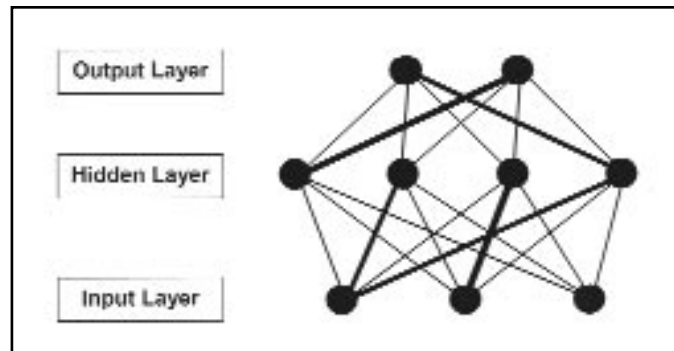


Fig. 3 — Schematic diagram showing the neural network structure, with three layers of nodes and connections between nodes.

### Neural Networks and FNN 1999

A brief description of neural networks in general, and the previously developed composition-only neural network model for ferrite prediction, FNN-1999, will be given here to provide a background for the extension of this model to include cooling rate effects. The reader is referred to the earlier papers (Refs. 13, 14) and other publications (Refs. 25, 26) for further details on neural networks. Neural networks are sophisticated nonlinear regression routines that, when properly “trained,” allow for the identification of complex relationships between a series of inputs and one or more outputs. These relationships are derived by means of connections between the inputs and an intermediate stage known as a hidden layer, and between this hidden layer and the outputs. This structure is shown schematically in Fig. 3. Simply put, values of the hidden nodes are determined by taking a weighted sum over all the inputs and, in turn, the outputs are determined by the weighted sum over all the hidden nodes. The weighted sums are converted by a transfer function before providing values to the next layer. The weights assigned to each input-hidden node connection, and each hidden node-output connection are determined by a training process and the different weights are depicted schematically by the differently weighted lines in Fig. 3. The network is trained with a training dataset that consists of numerous sets of input values and the corresponding outputs. The training process involves a comparison of the predicted outputs with the true outputs followed by a correction to the weight parameters. This process is repeated thousands of times, going through all the input/output pairs in the training dataset, until a reasonably accurate final network is determined. It must be kept in mind that although, in principle, a unique, optimum best network may exist, the training process will only approach this absolute best network without ever reach-

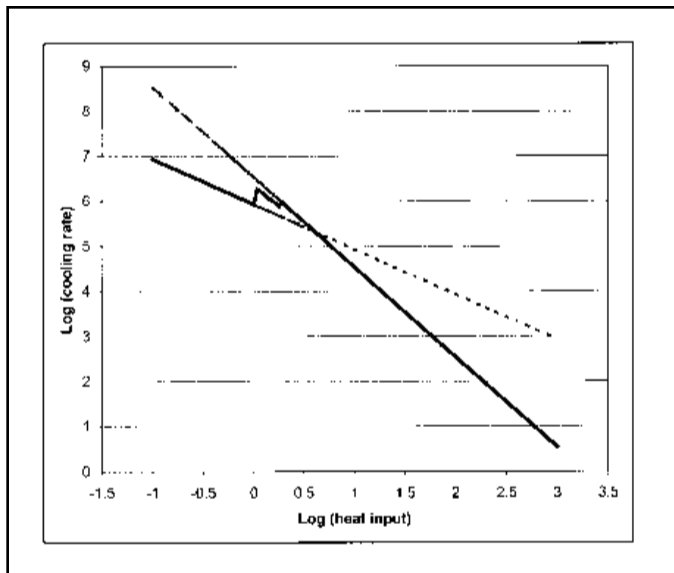


Fig. 4 — Example of calculated cooling rate vs. heat input using Equations 4 and 5. Long-dash line is for 2-D cooling condition, short-dash line is for 3-D cooling condition, and heavy solid line is cooling rate that is used over the entire heat input range.

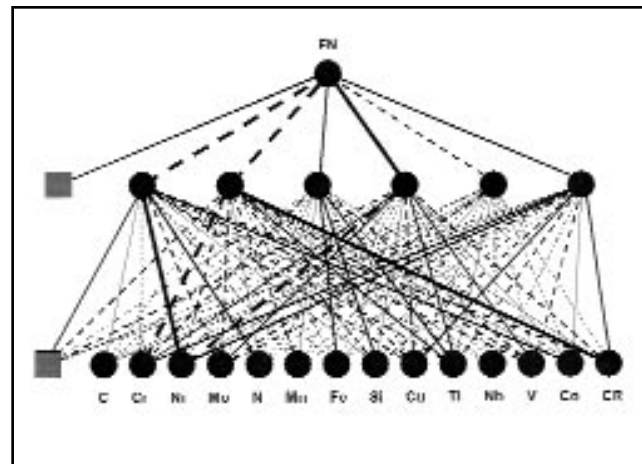


Fig. 5 — Final ORFN neural network model structure. The square nodes represent bias nodes corresponding to a constant input. Dashed lines represent negative weights between nodes while solid lines signify positive weights. Line thicknesses correspond to different ranges for the absolute values for the connecting weights: thin lines correspond to weights (absolute values) of 0 to <1.0; medium thickness lines represent weights from 1 to <4.0; thick lines correspond to weights  $\geq 4.0$ .

ing it. It will always be possible to derive a slightly better network by, for example, training longer or using additional data. The extent to which this ideal end result will be reached will depend upon the reliability of the data, the starting point for the analysis, the level of accuracy required, and numerous other factors. Thus, a unique final neural network is not produced. This point will be discussed again later, when the results of this analysis are presented.

The earlier composition-only neural network model, FNN-1999, consisted of 13 input nodes, 6 hidden nodes, and 1 output node. The input nodes corresponded to the concentrations, in wt-%, of 13 elements (Fe, Cr, Ni, C, N, Mo, Mn, Si, Cu, Ti, Nb, V, and Co). The ranges of these elements are given in Table 1. The choice of 6 hidden nodes was based on an analysis that showed this number of nodes was the smallest number of nodes (simple networks are preferred) that still provided good predictability (see Ref. 13). There was a single output node, the Ferrite Number (FN). Ferrite Number was used as the indicator of ferrite content since this is the most commonly used, and preferred, parameter (Ref. 27). In addition to the improved overall FN predictability of FNN-1999 compared to the WRC-1992 diagram, the earlier neural network model showed a composition dependence for the effect of alloying elements. This will not be described here, but the reader is referred to Ref. 14 for further details and examples showing this composition dependence.

The present ORFN model is similar in architecture to the earlier FNN-1999. A

14th input node was added for cooling rate. The cooling rate was calculated in units of  $^{\circ}\text{C}/\text{s}$ , but the logarithm of the cooling rate was used as the input to the neural network model since the cooling rate spanned several orders of magnitude. Six hidden nodes were used, as in FNN-1999. The choice of six nodes is explained later. The ranges of composition and cooling rates for training the present model are also listed in Table 1. It can be seen that the concentration ranges are essentially identical to FNN-1999; only the maximum Fe, N, and Co concentrations are marginally different.

## Dataset Generation

Development of a successful neural network to accurately describe a relationship such as that desired here between composition/cooling rate and FN depends on the availability of an extensive dataset for training the neural network. Such a dataset should span a wide range of input variables since the validity of the network predictions will be limited by the range of inputs over which it was trained. As such, it was imperative the extensive dataset used for the development of the WRC-1992 constitution diagram as well as the FNN-1999 neural network model (WRC dataset) be used since it contained nearly 1000 data points for composition and FN. These data were supplemented with the data generated earlier by David, Vitek, and Hebble (Ref. 18) for laser beam welds made on 14 different stainless steel alloys and heats as a function of laser power and welding speed (DVH dataset).<sup>2</sup> Finally,

new data were generated for several austenitic and duplex stainless steels (NEW dataset). These steels were autogenously welded using several different weld processes (arc welding and laser beam welding), weld power levels, and weld speeds (details provided later in this section). The combination of these three data sources provided a large dataset (1196 points in all) covering a wide range of compositions and cooling rates. The consolidation of these three datasets presented some significant problems in terms of consistency of data with regard to ferrite content and cooling rates. These issues are discussed in detail below.

## FN Values

As mentioned above and described elsewhere (Ref. 27), FN is the preferred indicator for ferrite level. This was used in the WRC dataset. However, in many cases, determination of FN in welds is impractical or impossible. For example, under the high cooling rate conditions achieved during laser beam welding, the weld bead is quite small, both in terms of weld bead width and weld depth. For such small welds, magnetic measurements of FN are inappropriate and inaccurate. This problem is exacerbated as the welding speed increases and the weld bead size decreases accordingly. The problem of making FN measurements on small samples was noted by Elmer and Eagar (Ref. 28).

2. The data from Ref. 18 for Alloy 446 were not used since its Ni content was only 0.34, which is significantly lower than the other data used for training the neural network.

They developed a vibrating sample magnetometer device for making measurements on small samples, but this method was not available. Therefore, volume-percent (vol-%) ferrite was measured metallographically in the DVH dataset and a means for converting vol-% ferrite to FN was needed. In the NEW dataset, a mix of FN and vol-% ferrite measurements was made and, once again, conversion to FN was required for many data points. In some cases, when generating the new data, multiple side-by-side overlapping laser weld runs were made in order to produce a wider weld zone that could be used for direct FN measurements.

The approach that was adapted for converting vol-% ferrite to FN relied on the concept of an extended ferrite number (Ref. 29). It was shown that the maximum FN for a 100% ferritic material is a function of the Fe content of the material. Several different expressions for maximum FN as a function of Fe content were proposed (Ref. 29) and the following equation was used:

$$FN_{max} = -0.025813 (Fe)^2 + 5.408679(Fe) - 102.3902 \quad (2)$$

where (*Fe*) is the wt-% of Fe in the alloy. Kotecki (Ref. 27) showed that a simple 1:1 relationship between the volume % (vol-%) ferrite and the normalized FN (= FN/FN<sub>max</sub>) is reasonable. Therefore, one can convert vol-% ferrite to FN by combining such a 1:1 relationship with Equation 2, yielding the following expression:

$$FN = (vol\text{-}\% \text{ ferrite}) \times (-0.025813 (Fe)^2 + 5.408679 (Fe) - 102.3902) / 100 \quad (3)$$

Clearly there are many sources of potential errors in using this conversion relationship. The potential errors in metallographic measurements of the vol-% ferrite have been noted in the literature (Ref. 27). The relationship between FN<sub>max</sub> and Fe content is subject to error as well. For example, Kotecki noted the relationship is dependent upon the instrument that is used (Ref. 29). Finally, Kotecki noted the conversion from normalized FN to vol-% ferrite is not strictly 1:1 (Ref. 27). Nonetheless, Equation 3 is considered to be sufficiently accurate. It was checked against other data available in the literature and good agreement was found. Since the need for converting vol-% ferrite to FN was unavoidable, the conversion used in Equation 3 was implemented. It should be noted there are numerous other sources of error in the prediction of FN, including errors in the datasets with regard to composition analyses, FN mea-

**Table 1 — Composition and Cooling Rate Ranges in Datasets Used for Training Ferrite Prediction Models**

Input Data	Model				
	FNN-1999		ORFN		
	min.	max	min.	max	
Concentration (wt-%)	Fe	45.60	72.51	45.60	72.52
	Cr	14.74	32	14.74	32
	Ni	4.61	33.5	4.61	33.5
	C	0.008	0.2	0.008	0.2
	N	0.01	0.3	0.01	0.33
	Mo	0.01	6.85	0.01	6.85
	Mn	0.35	12.67	0.35	12.67
	Si	0.03	1.3	0.03	1.3
	Cu	0.0	3.04	0.0	3.04
	Ti	0.0	0.54	0.0	0.54
	Nb	0.0	0.88	0.0	0.88
	V	0.0	0.23	0.0	0.23
	Co	0.0	0.32	0.0	0.45
Log Cooling Rate (°C/s)	—	—	1.00	6.54	

**Table 2 — Parameters Used in the Calculation of Cooling Rates, According to Equations 4(a) and 4(b)**

Parameter	Value	Reference
K (thermal conductivity)	0.28 watt/cm-°C	32
$\rho C_p$ (density x specific heat)	4.6 J/cm <sup>3</sup> -°C	32, 33
T' (temperature at which cooling rate is calculated)	1450°C	—
T <sub>0</sub> (initial plate temperature, ambient temperature)	25°C	—

surements, and errors in the cooling rate evaluation, as noted below. With this in mind, the conversion errors noted above are acceptable and expected to be comparable to (or smaller than) the errors from other sources.

### Cooling Rate Determination

A cooling rate associated with each composition and FN value is needed as input for the predictive model. Several practical considerations were taken into account before determining how to calculate the cooling rates. First and foremost, for both training the model and for the routine utilization of the final predictive model, a simple method for calculating cooling rate was needed. Therefore, elaborate heat and fluid flow models for welding that have been developed over the last two decades were immediately eliminated from consideration. Second, the methodology must allow for different cooling conditions that depend upon sample size. Thus, for thin sheet samples where the weld depth is comparable to the sheet thickness, two-dimension (2-D) cooling conditions prevail, whereas in thicker samples (relative to the weld pool depth), three-dimension (3-D) cooling conditions are present. One additional factor must also be considered. The accuracy of the cooling rate calculation is not critical to

achieve an accurate prediction model. Instead, what is necessary is that the cooling rates for different conditions must be ranked properly with respect to one another, and the cooling rates must be consistent with the data with which the network was trained. For example, although the absolute value for the cooling rate in a laser welded sample is not required, the assigned cooling rate must be properly ranked with respect to another weld, made on a different sample thickness, or with a different welding speed, power, or process. This consideration requires that all cooling rates be calculated in the same, consistent manner. Thus, actual cooling rate measurements are not appropriate as inputs; instead calculated cooling rates must be used throughout.

The analytical expressions for the cooling rate that were used are those derived by Adams (Ref. 30), based on the solutions of Rosenthal (Ref. 31) for heat conduction as applied to welding. These same expressions were used by David et al. (Ref. 18) for their extensive series of laser welds on stainless steels. However, David et al. only considered 3-D cooling conditions. This was reasonable in their work since most, but not all, of their laser welds resulted in only partial penetration welds. In contrast, in the present work, a broader perspective that includes 2-D cooling was needed. The relevant expressions for 2-D and 3-D cool-

**Table 3 — Alloys Used to Generate the “New” Dataset and Their Compositions (wt-%)**

Alloy	Fe	Cr	Ni	C	N	Mo	Mn	Si	Cu	Ti	Nb	V	Co
304A <sup>(a)</sup>	69.058	18.84	9.58	0.058	0.028	0.11	1.45	0.52	0.14	0.01	0 <sup>(b)</sup>	0.04	0.12
304B <sup>(a)</sup>	70.258	18.29	8.7	0.066	0.018	0.15	1.31	0.74	0.15	0 <sup>(b)</sup>	0.01	0.05	0.22
308A <sup>(a)</sup>	67.744	20.04	9.9	0.052	0.013	0.02	1.65	0.38	0.06	0 <sup>(b)</sup>	0 <sup>(b)</sup>	0.05	0.06
308B <sup>(a)</sup>	65.87	20.15	10.68	0.059	0.026	0.01 <sup>(b)</sup>	1.92	0.78	0.01	0.38	0 <sup>(b)</sup>	0.04	0.02
309A <sup>(a)</sup>	60.398	23.8	12.86	0.052	0.052	0.23	1.87	0.41	0.12	0 <sup>(b)</sup>	0.01	0.03	0.12
309B <sup>(a)</sup>	59.632	23.36	14.05	0.018	0.03	0.03	2.21	0.39	0.01	0.11	0.01	0.08	0.04
310A <sup>(a)</sup>	49.797	26.73	21.15	0.11	0.01 <sup>(b)</sup>	0.05	1.64	0.5	0 <sup>(b)</sup>				
310B <sup>(a)</sup>	53.682	25.62	19.18	0.03	0.01 <sup>(b)</sup>	0.15	0.9	0.42	0 <sup>(b)</sup>				
312A <sup>(a)</sup>	60.688	28.92	8.44	0.13	0.01 <sup>(b)</sup>	0.15	1.24	0.43	0 <sup>(b)</sup>				
312B <sup>(a)</sup>	59.09	29.72	8.78	0.11	0.01 <sup>(b)</sup>	0.2	1.68	0.39	0 <sup>(b)</sup>				
316A <sup>(a)</sup>	66.488	17.01	11.44	0.04	0.022	2.3	1.95	0.3	0.19	0 <sup>(b)</sup>	0.01	0.04	0.17
316B <sup>(a)</sup>	62.486	19.07	12.85	0.042	0.019	2.3	2.21	0.51	0.04	0.31	0.01	0.02	0.03
347A <sup>(a)</sup>	67.502	19.5	10	0.06	0.01 <sup>(b)</sup>	0.1	1.5	0.6	0 <sup>(b)</sup>	0 <sup>(b)</sup>	0.7	0 <sup>(b)</sup>	0 <sup>(b)</sup>
347B <sup>(a)</sup>	70.271	19.38	8.66	0.04	0.01 <sup>(b)</sup>	0.05	1.21	0.35	0 <sup>(b)</sup>				
S20910	57.197	21.25	13.26	0.027	0.33	2.14	4.97	0.29	0.14	0 <sup>(b)</sup>	0.19	0.18	0 <sup>(b)</sup>
S21904	62.74	19.54	7.18	0.017	0.29	0.4	9.4	0.34	0.07	0 <sup>(b)</sup>	0 <sup>(b)</sup>	0 <sup>(b)</sup>	0 <sup>(b)</sup>
308LT1	68.232	19.01	9.83	0.036	0.12	0.32	1.23	0.59	0.36	0.03	0.01	0.081	0.12
309LT1	59.509	23.96	13.03	0.027	0.19	0.42	1.34	0.78	0.38	0.033	0.02	0.08	0.17
316LT1	64.872	17.62	12.06	0.03	0.049	2.49	1.48	0.49	0.34	0.017	0.01	0.051	0.45
2209	63.226	23.166	9.195	0.028	0.128	2.86	0.886	0.405	0.047	0 <sup>(b)</sup>	0.012	0 <sup>(b)</sup>	0 <sup>(b)</sup>
2209Wa	61.5952	24.6	8.94	0.0248	0.177	3.23	0.74	0.4	0.13	0 <sup>(b)</sup>	0 <sup>(b)</sup>	0 <sup>(b)</sup>	0.13
2209Wb	59.7412	24.6	8.97	0.0248	0.171	3.19	0.77	0.41	1.96	0 <sup>(b)</sup>	0 <sup>(b)</sup>	0 <sup>(b)</sup>	0.13
2209Wc	59.5253	24.8	8.96	0.0237	0.178	3.22	0.76	0.42	1.95	0 <sup>(b)</sup>	0 <sup>(b)</sup>	0 <sup>(b)</sup>	0.13
2507	64.386	23.061	6.945	0.023	0.28 <sup>(b)</sup>	3.819	0.747	0.229	0.338	0 <sup>(b)</sup>	0.015	0 <sup>(b)</sup>	0.118
2507W	60.506	24.833	9.477	0.026	0.215	3.821	0.511	0.443	0.126	0 <sup>(b)</sup>	0 <sup>(b)</sup>	0 <sup>(b)</sup>	0 <sup>(b)</sup>
2553Wa	63.639	22.4	9.06	0.029	0.164	3.11	0.89	0.39	0.22	0 <sup>(b)</sup>	0.03	0 <sup>(b)</sup>	0.04
2553Wb	63.436	22.46	9.12	0.029	0.166	3.22	0.87	0.39	0.21	0 <sup>(b)</sup>	0.03	0 <sup>(b)</sup>	0.04
2553Wc	63.585	22.4	9.09	0.03	0.166	3.16	0.88	0.39	0.2	0 <sup>(b)</sup>	0.03	0 <sup>(b)</sup>	0.04
4462	66.895	21.988	5.881	0.022	0.168	2.968	1.42	0.455	0.169	0 <sup>(b)</sup>	0 <sup>(b)</sup>	0 <sup>(b)</sup>	0 <sup>(b)</sup>
4462W	63.599	22.67	8.178	0.024	0.167	3.165	1.625	0.437	0.104	0 <sup>(b)</sup>	0 <sup>(b)</sup>	0 <sup>(b)</sup>	0 <sup>(b)</sup>
Z100	64.385	22.857	7.261	0.034	0.227	3.571	0.757	0.193	0.672	0 <sup>(b)</sup>	0 <sup>(b)</sup>	0 <sup>(b)</sup>	0 <sup>(b)</sup>
Z100Wa	58.035	25.4	10.05	0.03	0.248	3.56	0.67	0.42	0.7	0 <sup>(b)</sup>	0.04	0.1	0.07
Z100Wb	57.995	25.4	9.97	0.028	0.251	3.67	0.64	0.42	0.72	0 <sup>(b)</sup>	0.04	0.1	0.07
Z100Wc	58.081	25.3	9.98	0.033	0.251	3.61	0.67	0.43	0.022	0 <sup>(b)</sup>	0.04	0.1	0.07

(a) Same alloy that was used in Ref. 18.

(b) Value was assigned since chemical analysis was not available. See text for further explanation.

ing rates are given in Equations 4(a) and 4(b), respectively.

$$\dot{T}_{2D} = 2\pi K \rho C_p (Vt/q)^2 (T' - T_o)^3 \quad 4(a)$$

$$\dot{T}_{3D} = 2\pi K (V/q) (T' - T_o)^2 \quad 4(b)$$

where  $\dot{T}$  = cooling rate (°C/s),  $K$  = thermal conductivity (watts/cm-°C),  $\rho$  = density (gm/cm<sup>3</sup>),  $C_p$  = specific heat (J/gm-°C),  $V$  = weld velocity (cm/s),  $t$  = thickness (cm),  $q$  = heat source power (watts),  $T'$  = temperature at which the cooling rate is calculated (°C), and  $T_o$  = initial plate temperature (°C). The values of the variables used in the calculations are given in Table 2. It should be noted constant values for the thermophysical properties were used in spite of the fact the values will depend upon alloy composition and the relative amounts of ferrite and austenite. Furthermore, cooling rates were calculated at a constant temperature ( $T'$ ) of 1450°C that corresponds roughly to the liquidus temperature. The ambient, initial plate temperature,  $T_o$ , was taken as 25°C. While calculating the cooling rate at the liquidus temperature may be appropriate for describing behavior related to solidification

conditions, the cooling rate at a lower temperature may be more appropriate for describing behavior related to the solid-state ferrite-to-austenite transformation. However, given a 2-D or 3-D condition, the ranking of cooling rates for different conditions will be the same regardless of the temperature at which the cooling rate is evaluated, and so one temperature for assessing cooling rates (1450°C) was used to quantify cooling rate effects due to both solidification and solid-state transformation behavior.

A procedure was needed to allow for a continuous transition in calculated cooling rate from a 2-D to a 3-D condition as the thickness or weld conditions changed. The recommended procedure described in the *Welding Handbook* (Ref. 32) uses a factor  $\tau$ , called the “relative plate thickness.”  $\tau$  is derived from the condition where the 2-D and 3-D cooling rates are equal and is defined as  $\tau = \sqrt{(\rho C_p V (T' - T_o) / q)}$ . According to Ref. 32, if  $\tau < 0.6$ , then the 2-D equation is appropriate, while if  $\tau > 0.9$ , then 3-D cooling prevails. Between these two limits, the cooling rate is between the 2-D and 3-D bounds. After examining many weld cross-

sections, it was found this criterion was not optimal. For many cases,  $\tau$  was found to be greater than 0.9, which should correspond to 3-D cooling according to the above criterion, and yet the weld penetration was > 90%, indicating 2-D cooling conditions prevailed. Therefore, a different criterion for choosing between the 2-D or 3-D cooling rate equations was used. This new criterion was

if  $\tau < 1.5$ , 2-D cooling rate was used 5(a)  
 if  $\tau > 2.0$ , 3-D cooling rate was used 5(b)  
 if  $1.5 < \tau < 2.0$ , the average of 2-D and 3-D cooling rate was used 5(c)

An example of how the calculated cooling rate varies as a function of heat input (power ÷ speed) is shown in Fig. 4. At low heat input, the 3-D cooling rate applies. Over the heat input range of 1 to 2 (log[heat input] varies from 0 to 0.3), the average cooling rate is used, and for higher heat inputs, the 2-D cooling rate applies. Although the variation of cooling rate with heat input does not behave monotonically, the slightly irregular behavior when using the average cooling rate cannot be avoided and is not considered to be

crucial. The transition from 2-D to 3-D cooling rates shown in Fig. 4 depends on the thickness that is used; as the thickness increases, the transition shifts to higher heat inputs.

Perhaps the most serious assumption that was made was related to the cooling rates that were used for the WRC dataset. This dataset made up 80% of the total dataset and, therefore, it was essential to include these data when training the neural network in order to achieve a robust predictive model that was valid and accurate over a large composition range. However, there were no details regarding the welding conditions (such as power, speed, thickness) that were used to generate this dataset, and so it was impossible to calculate a cooling rate for this critical and dominant component of the entire dataset. In order to utilize this extensive dataset, a "default" cooling rate of 10°C/s was assigned to all the data in the WRC dataset. This value is reasonable since the WRC dataset consisted of data from arc welds only and was generated under "conventional" conditions, so it is unlikely that high weld speeds were used, or that high cooling rate conditions prevailed.

There are significant sources of error in generating the cooling rate as an input variable. When the cooling rate was calculated, errors may arise from any or all of the following sources:

- 1) The same thermal property parameters were used regardless of alloy composition or the relative amounts of ferrite and austenite.

- 2) The transition from 2-D to 3-D cooling yielded a nonmonotonic variation in cooling rate with increasing heat input.

- 3) The effect of weld composition on weld penetration, such as that due to variations in the magnitude and direction of the Marangoni-induced fluid flow, were ignored.

- 4) A default cooling rate was "assigned" to a large portion of the data. However, in order to produce a model that can be readily used, many of these simplifications and assumptions were unavoidable. The use of LOG(cooling rate) as a variable reduces the sensitivity of the model to cooling rate to some degree. In addition, as will be shown later, the changes in FN as a function of cooling rate occur over several orders of magnitude in cooling rate and, therefore, the accuracy in the cooling rate calculation is not quite so critical; an "order of magnitude" accuracy may be acceptable.

#### Procedures for Generating New Data

New welds were made from several alloys and welding conditions to supplement the high cooling rate data available in the

DVH dataset. In particular, duplex stainless steel compositions were examined as well as standard austenitic stainless steel compositions. A list of alloys and their compositions is given in Table 3. Several of the alloys were the same as those used in Ref. 18, as noted in the table. These alloys were in the form of 0.51-mm-thick sheet. New composition analyses were used to include many of the elements needed in the neural network model. Additional alloys were in the form of plate or weld pads. The weld pads are denoted with a "W" in the alloy designation in Table 3. For many elemental concentrations, chemical analysis data were not available so minimum default values appropriate for the neural network were used. A detailed explanation of the minimum default values is given in Ref. 13. These concentrations are also marked in the table. One exception was for the nitrogen content in Alloy 2507 (plate). For this material, no nitrogen analysis was available, but assignment of a minimum concentration of 0.01 was inappropriate since the alloy specification requires a significant nitrogen level. Therefore, a nominal value of 0.28 was used, which is between the alloy specification limits of 0.24 and 0.32. Assigning such a value, rather than 0.01, was supported by the fact the 2507 weld pad had a nitrogen content of 0.215.

Autogenous GTA and pulsed Nd:YAG laser beam welds were made on the alloys listed in Table 3 for a range of power levels and welding speeds to generate the data used to supplement the WRC and DVH datasets. The preferred method for assessing the ferrite content was by measuring the FN using a Fischer Feritscope. This was possible for the thick plate material and weld pads. When the autogenous welds were narrow (high-speed arc welds or laser welds), multiple passes were made side by side to obtain a wider weld region that could be analyzed with the Feritscope. For the sheet material, measuring the FN directly was inappropriate since the sheet was too thin. Therefore, vol-% ferrite was determined and these values were converted to FN using Equation 3.

Cooling rates were calculated using the procedure described earlier. For the case of pulsed Nd:YAG laser beam welds, an additional term for the absorptivity/efficiency was needed when specifying the power levels. A value of 20% was used, the same value that was used in Ref. 18.

#### Network Development

In the present analysis, a feed-forward network with a back-propagation optimization scheme was utilized (Ref. 26). A commercial software package (*Neural-Works Professional II/PLUS*) was used for

the neural network development (Ref. 34). At the onset, a determination was required as to whether to use the FNN-1999 composition-only neural network model as a starting point for the new model that includes cooling rate or to develop a new network from scratch. In addition, regardless of the starting point, an analysis of the optimum network architecture, i.e., the optimum number of hidden nodes, was required. These two issues were addressed by performing a series of preliminary analyses using a combination of the WRC dataset and the DVH dataset. The procedure was the same as that described in detail in Ref. 13. For the case where the FNN-1999 model was used as the starting point, architectures with six or more hidden nodes were considered (FNN-1999 had six hidden nodes). For the case of a "from scratch" network, architectures with one or more hidden nodes were examined. It was determined that developing the new network with the FNN-1999 as a starting point did not result in greater accuracies or computational efficiencies. Therefore, the new cooling-rate inclusive network was developed from scratch. Furthermore, it was found that all networks with six or more hidden nodes had comparable prediction accuracies so the simplest, six-node architecture was adapted.

The final network was developed by using all the available data (WRC + DVH + NEW datasets) for training and it is shown schematically in Fig. 5. The parameters for the network are given in Part 2 (Ref. 24). Four hundred different networks were calculated, using 200 different random seed numbers that define the starting weights and the order in which the data are examined during training, and two different random arrangements of the data. As mentioned earlier, from a practical point of view, a unique "best" network is never derived. Instead, the best network among the 400 networks that were trained was chosen. A measure of the accuracy with which the network fits the training dataset is given by the root mean square (RMS) error between the predicted (Pred) value and the experimental (Exp) value.<sup>3</sup> The lowest RMS, corresponding to the best of the 400 trial networks, was 4.70. Many of the 400 trial networks had comparable RMS errors. Four other networks had RMS values within 2% of the minimum, and the average RMS of all 400 networks was only 13% higher than the lowest value of 4.70. Thus, although the training process did not produce a unique final neural network, many of the networks that were calculated were of comparable accuracy. "Committees" with up to 15 of the best networks were also evaluated, where the average of the predictions

3.  $RMS = \sqrt{(\sum(\text{ExpFN} - \text{Pred FN})^2) / 1196}$

of the networks in the committee was used. However, the committee predictions were only marginally better than the predictions from the single best network and so the simpler, single network model was used. The prediction accuracy of the network, evaluated by several means, as well as sample results and comparisons with other models, are detailed in Part 2 (Ref. 24).

## Summary and Conclusions

A neural network model was developed for predicting Ferrite Number (FN) in stainless steel welds as a function of cooling rate and composition. This new model, called ORFN (Oak Ridge Ferrite Number), allows, for the first time, for the prediction of FN as a function of composition and weld process conditions (weld speed, welding power, material thickness) for both conventional arc welding and more rapid cooling rate processes such as laser beam welding. A large dataset consisting of previously published data as well as newly generated data was used to develop the model.

Procedures were identified to convert vol-% ferrite measurements to FN and to calculate cooling rates as a function of welding conditions for both 2-D and 3-D cooling conditions. The optimum network architecture was found to consist of six hidden nodes. The model is evaluated in terms of its accuracy and its predictability in Part 2 (Ref. 24).

### Acknowledgments

The authors would like to thank Y. Iskander for help with the neural network development in the early stages of this program. R. Reed, Oak Ridge National Laboratory, is thanked for preparing many of the welds in this study. The authors would like to thank the following people for providing materials for generating new data: D. Kotecki, The Lincoln Electric Company, Cleveland, Ohio; F. Lake, ESAB Welding and Cutting Products, Hanover, Pa.; S. Jana, Hobart Brothers, Troy, Ohio; and R. Gower, Carpenter Technology Corporation, Reading, Pa. The authors would like to acknowledge the ERULF program of the U.S. Department of Energy, administered by Oak Ridge Associated Universities, Oak Ridge, Tenn., for providing the means for one of the authors (CRH) to participate in this research. This research was sponsored by the Division of Materials Sciences and Engineering, U.S. Department of Energy, and the Office of Science, Laboratory Technology Research Program, U.S. Department of Energy, under contract DE-AC05-00OR22725 with UT-Battelle, LLC.

### References

- Schaeffler, A. 1949. Constitution diagram for stainless steel weld metal. *Metal Progress* 56: 680-680B.
- Hull, F. C. 1973. Delta ferrite and martensite formation in stainless steels. *Welding Journal* 52(5): 193-s to 203-s.
- DeLong, W. T. 1974. Ferrite in austenitic stainless steel weld metal. *Welding Journal* 53(7): 273-s to 286-s.
- Kakhovskii, N. I., Lipodaev, V. N., and Fadeeva, G. V. 1985. The arc welding of stable austenitic corrosion-resisting steels and alloys. *Avt. Svarka*, 5: 55 to 57.
- Olson, D. L. 1985. Prediction of austenitic weld metal microstructure and properties. *Welding Journal* 64(10): 281-s to 295-s.
- Siewert, T. A., McCowan, C. N., and Olson, D. L. 1988. Ferrite number prediction to 100 FN in stainless steel weld metal. *Welding Journal* 67(12): 289-s to 298-s.
- Kotecki, D. J., and Siewert, T. A. 1992. WRC-1992 constitution diagram for stainless steel weld metals: a modification of the WRC-1988 diagram. *Welding Journal* 71: 171-s to 178-s.
- Schneider, H. 1960. Investment casting of high-hot strength 12% chrome steel. *Foundry Trade Journal* 108: 562-563.
- Schoefer, E. A. 1974. Appendix to Mössbauer effect examination of ferrite in stainless steel welds and castings. *Welding Journal* 53: 10-s to 12-s.
- Szumachowski, E. R., and Kotecki, D. J. 1984. Effect of manganese on stainless steel weld metal ferrite. *Welding Journal* 63(5): 156-s to 161-s.
- Self, J. A., Matlock, D. K., and Olson, D. L. 1984. An evaluation of austenitic Fe-Mn-Ni weld metal for dissimilar metal welding. *Welding Journal* 63(9): 282-s to 288-s.
- Babu, S. S., Vitek, J. M., Iskander, Y. S., and David, S. A. 1997. New model for prediction of ferrite number of stainless steel welds. *Science and Technology of Welding and Joining* 2(6): 279-285.
- Vitek, J. M., Iskander, Y. S., and Oblow, E. M. 2000. Improved ferrite number prediction in stainless steel arc welds using artificial neural networks — Part 1: neural network development. *Welding Journal* 79(2): 33-s to 40-s.
- Vitek, J. M., Iskander, Y. S., and Oblow, E. M. 2000. Improved ferrite number prediction in stainless steel arc welds using artificial neural networks — Part 2: neural network results. *Welding Journal* 79(2): 41-s to 50-s.
- Vasudevan, M., Muruganath, M., and Bhaduri, A. K. 2002. Application of Bayesian neural network for modeling and prediction of ferrite number in austenitic stainless steel welds. *Mathematical Modelling of Weld Phenomena*, 6, ed. H. Cerjak, Institute of Materials, London, pp. 1079 - 1099.
- Vitek, J. M., DasGupta, A., and David, S. A. 1983. Microstructural modification of austenitic stainless steels by rapid solidification. *Metallurgical Transactions* 14A: 1833-1841.
- Katayama, S., and Matsunawa, A. 1984. Solidification microstructure of laser welded stainless steels. *Proc. of ICALCO 84*, Boston, Mass. 44: 60-67.
- David, S. A., Vitek, J. M., and Hebble, T. L. 1987. Effect of rapid solidification on stainless steel weld metal microstructures and its implications on the Schaeffler diagram. *Welding Journal* 66(10): 289-s to 300-s.
- Bobadilla, M., Lacaze, J., and Lesoult, G. 1988. Influence des conditions de solidification sur le déroulement de la solidification des aciers inoxydables austénitiques. *Journal of Crystal Growth* 89: 531-544.
- Elmer, J. W., Allen, S. M., and Eagar, T. W. 1989. Microstructural development during solidification of stainless steel alloys. *Metallurgical Transactions A* 20A: 2117 to 2131.
- Lippold, J. C. 1994. Solidification behavior and cracking susceptibility of pulsed laser welds in austenitic stainless steels. *Welding Journal* 73(6): 129-s to 139-s.
- Vitek, J. M., and David, S. A. 1994. Prediction of non-equilibrium solidification modes in austenitic stainless steel laser welds. *Laser Materials Processing IV*, eds. J. Mazumder, K. Mukerjee, and B. L. Mordike. Warrendale, Pa.: TMS, pp. 153-167.
- Koseki, T., and Flemings, M. C. 1997. Solidification of undercooled Fe-Cr-Ni alloys: Part III — phase selection in chill casting. *Metallurgical and Materials Transactions A* 28A: 2385-2395.
- Vitek, J. M., David, S. A., and Hinman, C. R. 2003. Improved ferrite number prediction model that accounts for cooling rate effects — Part 2: Model results. To be published in 82(2) *Welding Journal*.
- Rumelhart, D. E., Widrow, B., and Lehr, M. A. 1994. The basic ideas in neural networks. *Communications of the ACM* 37(3): 87-92.
- Bishop, C. M. 1994. Neural networks and their applications. *Review of Scientific Instruments* 65(6): 1803-1832.
- Kotecki, D. J. 1997. Ferrite determination in stainless steel welds — advances since 1974. *Welding Journal* 76(1): 24-s to 37-s.
- Elmer, J. W., and Eagar, T. W. 1990. Measuring the residual ferrite content of rapidly solidified stainless steel alloys. *Welding Journal* 69(4): 141-s to 150-s.
- Kotecki, D. J. 1982. Extension of the WRC Ferrite Number system. *Welding Journal* 61(11): 352-s to 361-s.
- Adams, C. M. 1958. Cooling rates and peak temperatures in fusion welding. *Welding Journal* 37(5): 210-s to 215-s.
- Rosenthal, D. 1941. Mathematical theory of heat distribution during cutting and welding. *Welding Journal* 20(5): 220-s to 234-s.
- Welding Handbook* Vol. 1, Welding Technology, 8th ed. 1987. Miami, Fla.: AWS, pp. 75-77.
- Kou S. 1987. *Welding Metallurgy*. New York, N.Y.: John Wiley and Sons, p. 39.
- NeuralWare, Inc., Pittsburgh, Pa. 1995.